Gas metallicity in the narrow-line regions
of high-redshift active galactic nuclei

T. Nagao[1,2], R. Maiolino[1], and A. Marconi[1]

[1] INAF - Osservatorio Astrofisico di Arcetri, Largo Enrico Fermi 5, 50125 Firenze, Italy
e-mail: [tohru;maiolino;marconi]@arcetri.astro.it
[2] National Astronomical Observatory of Japan, 2-21-1 Osawa, Mitaka, Tokyo 151-8588, Japan

ABSTRACT

We analyze optical (UV rest-frame) spectra of X-ray selected narrow-line QSOs at redshift $1.5 \lesssim z \lesssim 3.7$ found in the Chandra Deep Field South and of narrow-line radio galaxies at redshift $1.2 \lesssim z \lesssim 3.8$ to investigate the gas metallicity of the narrow-line regions and their evolution in this redshift range. Such spectra are also compared with UV spectra of local Seyfert 2 galaxies. The observational data are inconsistent with the predictions of shock models, suggesting that the narrow-line regions are mainly photoionized. The photoionization models with dust grains predict line flux ratios which are also in disagreement with most of the observed values, suggesting that the high-ionization part of the narrow-line regions (which is sampled by the available spectra) is dust-free. The photoionization dust-free models provide two possible scenarios which are consistent with the observed data: low-density gas clouds ($n_H \lesssim 10^3$ cm^{-3}) with a sub-solar metallicity ($0.2 \lesssim Z_{gas}/Z_\odot \lesssim 1.0$), or high-density gas clouds ($n_H \sim 10^5$ cm^{-3}) with a wide range of gas metallicity ($0.2 \lesssim Z_{gas}/Z_\odot \lesssim 5.0$). Regardless of the specific interpretation, the observational data do not show any evidence for a significant evolution of the gas metallicity in the narrow-line regions within the redshift range $1.2 \lesssim z \lesssim 3.8$. Instead, we find a trend for more luminous active galactic nuclei to have more metal-rich gas clouds (luminosity-metallicity relation), which is in agreement with the same finding in the studies of the broad-line regions. The lack of evolution for the gas metallicity of the narrow-line regions implies that the major epoch of star formation in the host galaxies of these active galactic nuclei is at $z \gtrsim 4$.

Key words. galaxies: active – galaxies: evolution – galaxies: nuclei – quasars: emission lines – quasars: general

1. Introduction

Understanding galaxy formation and evolution is one of the key astrophysical issues of this decade. The chemical composition of gas and stars in galaxies provides important information because it is a tracer of the star formation history in galaxies. A promising way to study the chemical evolution of galaxies is to measure their metallicity as a function of redshift. Since it is extremely hard and time-consuming to measure stellar metallicity of faint high-z galaxies, because high quality spectra of shallow absorption features are required (but see, e.g., Pettini et al. 2000; Mehlert et al. 2002), investigating the gas metallicity through emission lines is a promising strategy. However, most of the available diagnostic emission lines associated with massive star formation (e.g., [OII]λ3727, [OIII]$\lambda\lambda$4959,5007, [NII]λ6548,6583) are in the rest-frame optical wavelength and thus are shifted to near infrared in high-z galaxies. Accordingly, observations of these emission lines in high-z galaxies are feasible only for relatively bright targets (e.g., Teplitz et al. 2000; Pettini et al. 2001; Tecza et al. 2004; Shapley et al. 2004). Instead, active galactic nuclei (AGNs) exhibit bright emission lines at rest-frame UV wavelengths, which can be used to investigate the gas metallicity even in high-z objects. Spectroscopic observations of high-z QSOs

suggest that gas metallicity in the broad-line region (BLR) tends to be much higher than solar (e.g., Hamann & Ferland 1992; Dietrich et al. 2003; Nagao et al. 2006) reaching as much as $Z \sim 15\ Z_\odot$ (Baldwin et al. 2003). However it is not clear how the gas metallicity inferred from the broad lines is related to the chemical properties of the host galaxies, since the broad lines of AGNs sample only a very small region of galactic nuclei ($R_{BLR} \ll 1$ pc; e.g., Kaspi et al. 2000), which may have evolved more rapidly than the host galaxy.

An alternative possibility is to use narrow line AGNs. In this paper we focus on narrow-line AGNs at high redshift, in particular on high-z radio galaxies (HzRGs) and type-2 QSOs (QSO2s). The nuclei of narrow-line AGNs are thought to be obscured by edge-on optically thick tori (e.g., Antonucci & Miller 1985; Antonucci 1993; Cohen et al. 1999). Since the broad emission lines and the strong ionizing continuum are blocked by this "natural coronagraph", we can investigate narrow UV emission lines whose spatial extension is roughly comparable to that of the host galaxies ($\sim 10^{2-4}$ pc), without any complex deblending of broad and narrow components for the emission lines. Although narrow emission lines of HzRGs are often strongly influenced by a radio jet in terms of kinematics and morphological properties (e.g., McCarthy et al. 1991;

Baum & McCarthy 2000), the ionization mechanism is mostly dominated by photoionization, not by shock ionization (e.g., Villar-Martin et al. 1997; Allen et al. 1998; Iwamuro et al. 2003). Therefore, we can obtain information on the gas metallicity of the narrow-line regions (NLRs) by comparing the observed emission-line flux ratios with the predictions of photoionization models. By comparing the NLRs of HzRGs and QSO2s with low-z type 2 AGNs (Seyfert 2 galaxies; Sy2s), we can investigate whether the gas metallicity evolves on a cosmological timescale or not.

By focusing on the flux ratio of $NV\lambda1240/CIV\lambda1549$ that is one of the most frequently used metallicity diagnostics for AGNs (generally for the BLR; e.g., Hamann & Ferland 1992, 1999; Dietrich et al. 2003), De Breuck et al. (2000) reported gas metallicity of HzRGs in the range $0.4\ Z_\odot \lesssim Z_{gas} \lesssim 3.0\ Z_\odot$ or possibly even much higher (see also van Ojik et al. 1994; Vernet et al. 2001). They also claimed a metallicity evolution within their sample from $z > 3$ to $z < 3$: the gas metallicity of all HzRGs at $z > 3$ in their sample is $Z_{gas} < 2\ Z_\odot$, at variance with their sample at $z < 3$. Norman et al. (2002) reported that the strong $NV\lambda1240$ emission of a X-ray selected high-z QSO2 found in Chandra Deep Field South (CDFS; Giacconi et al. 2002; Rosati et al. 2002), CDFS-202 ($z \simeq 3.7$), is consistent with a super-solar metallicity of its NLR, and more specifically $Z_{gas} \sim 2.5$–$3.0\ Z_\odot$. However, since the $NV\lambda1240$ emission becomes very weak for metal-poor gas (i.e., $Z_{gas} \lesssim 1\ Z_\odot$), only upper-limit fluxes on $NV\lambda1240$ are available for the majority of the HzRG sample in De Breuck et al. (2000), which makes the investigation of the metallicity evolution difficult. An additional issue is that Iwamuro et al. (2003), based on rest-frame optical spectra obtained by sensitive near-infrared spectroscopy, recently reported that HzRGs at $2.0 < z < 2.6$ tend to show sub-solar metallicities ($Z_{gas} \sim 0.2\ Z_\odot$), significantly lower than values reported by De Breuck et al. (2000). Although it is clear that improved and additional observational data for a larger sample of HzRGs are required to reconcile this disagreement, both more sensitive measurements of $NV\lambda1240$ and deeper near-infrared spectroscopic data are very difficult to obtain for HzRGs and QSO2s.

To tackle these issues, it is useful to find alternative metallicity diagnostics that consists only of strong UV emission lines. In this paper, we investigate strong UV emission lines for HzRGs, QSO2s, and Sy2s. By comparing the compiled data with photoionization model calculations, we discuss the evolution of the gas metallicity of the NLRs in AGNs, from high-z to the local universe, using only strong UV emission lines. The compiled data and our photoionization model calculations are presented in Sect. 2 and Sect. 3, respectively. We compare the observational data with the model results, discuss the properties of NLR gas clouds and the implications for the chemical evolution of AGNs in Sect. 4. A brief summary is given in Sect. 5.

2. Data

2.1. Data compilation

To investigate the possible chemical evolution of the NLRs in AGNs, we compiled the fluxes of some strong UV emission

lines, $NV\lambda1240$, $CIV\lambda1549$, $HeII\lambda1640$ and $CIII]\lambda1909$. We focus only on these emission lines since fainter lines were measured only in a few type 2 AGNs. The details of the data compilation for each population of objects are given below.

(1) HzRGs: we used emission-line fluxes of HzRGs given by De Breuck et al. (2000), who compiled emission-line flux data of 165 radio galaxies from the literature. This sample contains 114 HzRGs at $1.2 \leq z \leq 3.8$ for which we can investigate the rest-frame UV spectra. We assigned the error on each line flux by checking the original references. For objects whose emission-line flux errors are not given in the original reference, we assigned a 20% error for each emission line. For emission-line fluxes measured with a statistical significance lower than 3σ, we adopted 3σ upper-limit values instead of the measured fluxes. We also referred to the measurements of emission-line flux data of 9 HzRGs presented by Vernet et al. (2001). Although these HzRGs are included in the sample of De Breuck et al. (2000), we adopted the data of Vernet et al. (2001) for these 9 HzRGs because of the higher signal-to-noise ratios of the Vernet et al. (2001) data. Accordingly, the number of HzRGs whose fluxes of $CIV\lambda1549$, $HeII\lambda1640$ and $CIII]\lambda1909$ are measured is 51 in total, of which two objects are lower- or upper-limit data.

(2) QSO2s: we used the spectra of X-ray selected QSO2s in CDFS recently obtained by Szokoly et al. (2004). Among 288 objects whose spectra were obtained with VLT/FORS by Szokoly et al. (2004), 51 objects are at $z > 1.2$. From these 51 objects, we selected 9 objects with a high quality spectrum that shows only narrow emission lines. All of these 9 objects (distributed at $1.54 \lesssim z \lesssim 3.70$; see Table 1) show strong $CIV\lambda1549$ emission which indicates, along with their X-ray emission, that these objects harbor an AGN (i.e., not starburst galaxies). We obtained spectral data of these 9 objects from the CDFS web site[1], and measured their emission-line fluxes and errors by means of a simple Gaussian fitting. The measured fluxes are given in Table 1. In this table fluxes of Lyα are also given for the reader's convenience, although we do not use the Lyα flux in the analysis and discussion in this paper. The reported errors do not take any possible systematic errors into account. In addition to the nine QSO2s in the CDFS, we also used the emission-line flux data of CXO J084837.9+445352 (CXO 52), a QSO2 at $z = 3.288$ found by Stern et al. (2002). Since the flux error for $NV\lambda1240$ is not given by Stern et al. (2002), we assigned a 20% error for this line as for the HzRGs mentioned above. Therefore the number of QSO2s is 10 in total.

(3) Sy2s: we compiled the flux data of 9 Sy2s observed by IUE from the literature. The object name, the compiled flux data and their errors and the reference are given in Table 2. For the data obtained by Thuan (1984), they reported UV emission-line fluxes for IC 5135, not only for NCG 5135; however, we do not include the data of IC 5135 because the signal-to-noise ratio is too low (see Thuan 1984 for details). For fluxes with no information on their errors in the reference, we assigned a 20% error as for the HzRGs and QSO2s (except for low-accuracy measurements explicitly mentioned in the reference for which

---

[1] http://www.mpe.mpg.de/CDFS/data/

Table 1. Emission-line measurements of X-ray selected QSO2s at $z > 1.2$.

Object	Redshift	Ly$\alpha\lambda$1216[a]	N$v\lambda$1240[a]	C$IV\lambda$1549[a]	He$II\lambda$1640[a]	CIII]λ1909[a]
CDFS–027	3.064	12.6 ± 0.7	2.5 ± 0.7	6.4 ± 0.5	2.3 ± 0.9	<2.9[c]
CDFS–031	1.603	—	—	24.1 ± 1.4	13.3 ± 1.2	10.3 ± 1.3
CDFS–057	2.562	112.2 ± 1.3	8.4 ± 1.4	17.8 ± 0.8	7.6 ± 0.8	13.3 ± 0.9
CDFS–112a	2.940	58.3 ± 0.5	14.6 ± 0.8	15.2 ± 1.0	8.9 ± 0.9	4.5 ± 0.8
CDFS–153	1.536	—	—	25.5 ± 1.4	6.2 ± 1.1	13.7 ± 1.6
CDFS–202	3.700	78.1 ± 1.0	26.8 ± 1.1	38.9 ± 1.2	19.7 ± 1.5	<12.9[c]
CDFS–263b	3.660	70.9 ± 0.7	4.6 ± 0.7	15.5 ± 0.8	<4.0[c]	<7.6[c]
CDFS–531	1.544	—	—	22.0 ± 1.4	17.4 ± 1.5	14.4 ± 1.5
CDFS–901	2.578	37.1 ± 0.6	6.5 ± 0.8	19.7 ± 1.0	<2.8[c]	3.3 ± 0.9
CXO 52[b]	3.288	189 ± 4	6 ± 1.2[d]	35 ± 2	17 ± 2	21 ± 2

[a] Fluxes are in units of 10^{-18} erg s^{-1} cm^{-2}.
[b] Data taken from Stern et al. (2002).
[c] 3σ upper-limit flux.
[d] The error was assigned by us; see text.

Table 2. Emission-line measurements of Sy2s.

Object	Redshift	Ly$\alpha\lambda$1216[a]	N$v\lambda$1240[a]	C$IV\lambda$1549[a]	He$II\lambda$1640[a]	CIII]λ1909[a]	Ref.[b]
NGC 1068	0.004	713 ± 100	224 ± 41	520 ± 80	187 ± 29	240 ± 35	1
NGC 4507[c]	0.012	75.6 ± 15.1	5.2 ± 1.0	13.5 ± 2.7	5.6 ± 1.1	5.8 ± 1.2	2
NGC 5135[c]	0.014	59.0 ± 11.8	1.1 ± 0.2	4.1 ± 0.8	10.0 ± 2.0	—	3
NGC 5506[c]	0.006	—	—	4.5 ± 1.4[d]	2.0 ± 0.6[d]	3.6 ± 0.7	2
NGC 7674	0.029	47.0 ± 20.3	—	11.4 ± 3.3	5.1 ± 1.5	7.9 ± 2.7	4
Mrk 3	0.014	64 ± 19[d]	3 ± 1[d]	21 ± 2	9 ± 1	9 ± 1	5
Mrk 573	0.017	151.2 ± 22.7	6.3 ± 0.9	29.0 ± 4.3	12.6 ± 1.9	8.8 ± 1.3	6
Mrk 1388	0.021	—	—	8.3 ± 1.2	3.8 ± 0.6	3.6 ± 0.5	6
MCG –3–34–64[c]	0.017	56 ± 11	5 ± 1	14 ± 3	10 ± 2	7 ± 1	7

[a] Fluxes are in units of 10^{-14} erg s^{-1} cm^{-2}.
[b] References. — (1) Snijders et al. (1986), (2) Bergeron et al. (1981), (3) Thuan (1984), (4) Kraemer et al. (1994), (5) Malkan & Oke (1983), (6) McAlpine (1988), (7) De Robertis et al. (1988).
[c] 20% of the line flux is assigned as the flux error.
[d] 30% of the line flux is assigned as the flux error.

we assigned a 30% error). All of the targets are at $z < 0.03$ and thus we regard this sample as representative of the NLRs in the local universe.

The redshift distributions of the HzRG and the QSO2 samples are shown in Fig. 1. The compiled data are not corrected for Galactic and intrinsic dust reddening. Possible effects of the reddening on our analysis are discussed later (Sect. 2.2). Since most of these data were obtained with low-dispersion spectroscopy, the measured CIII] flux may be contaminated by the SiIII]$\lambda\lambda$1883,1892 flux. However, the contribution of SiIII] is thought to be small and we will discuss this issue further in Sect. 3.2.

2.2. Compilation results

In Fig. 2a the compiled line flux ratios are plotted on the C$IV\lambda$1549/He$II\lambda$1640 versus CIII]λ1909/C$IV\lambda$1549 diagram. The C$IV\lambda$1549/He$II\lambda$1640 flux ratio is expected to be sensitive to the gas metallicity. This is because the gas temperature

decreases when the metallicity increases in low-density ($\lesssim 10^4$ cm^{-3}) gas clouds (e.g., Ferland et al. 1984) and thus the collisional excitation of CIV is gradually suppressed, while the He$II\lambda$1640 luminosity is basically proportional to the volume of the doubly-ionized helium region and thus rather insensitive to the gas metallicity. The CIII]λ1909/C$IV\lambda$1549 ratio is instead expected to be sensitive to the ionization degree of the gas clouds. Therefore, CIII]λ1909/C$IV\lambda$1549 can be used to check any dependence of C$IV\lambda$1549/He$II\lambda$1640 on the ionization state of the gas. Thus, a diagnostic diagram that consists of these two flux ratios is expected to be useful to estimate the properties of NLRs only with strong UV emission lines, as discussed more extensively in Sects. 3 and 4 (see also Groves et al. 2004b).

In Fig. 2 we also show the effect of the dust extinction on the line ratios, for the case of $A_V = 5.0$ mag. An extinction curve described by Cardelli et al. (1989) is adopted. Since the dust extinction in typical type 2 AGNs is generally $A_V \lesssim 3$ mag (see, e.g., Fig. 5 of Nagao et al. 2001b), we conclude that the
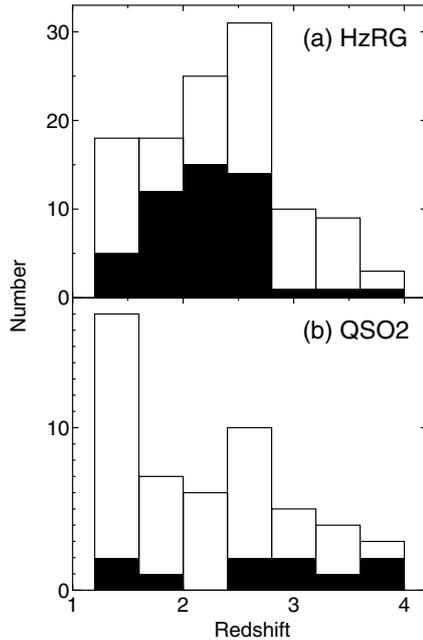
Fig. 1. Redshift distributions of the sample objects. **a)** The HzRG sample. The white histogram denotes the original HzRG sample (at $1.2 \leq z \leq 4.0$; 114 objects) of De Breuck et al. (2000) while the black histogram denotes the 49 HzRGs whose emission-line fluxes of $C_{IV}\lambda1549$, $He_{II}\lambda1640$ and $C_{III}]\lambda1909$ are measured. **b)** The QSO2 sample. The white histogram denotes the AGNs (including both broad-line and narrow-line AGNs) at $z \geq 1.2$ found in the CDFS (51 objects; Szokoly et al. 2004) and one additional QSO2 reported by Stern et al. (2002), while the black histogram denotes the narrow-line AGNs among them (10 objects) which are presented in Table 1.

Table 3. Averaged diagnostic flux ratios.

Sample	Number[a]	C IV / He II	C III] / C IV
HzRG	49	$1.42^{+0.10}_{-0.09}$	$0.67^{+0.06}_{-0.06}$
QSO2	6	$2.07^{+0.36}_{-0.31}$	$0.52^{+0.08}_{-0.07}$
Sy2	8	$2.20^{+0.16}_{-0.15}$	$0.49^{+0.06}_{-0.05}$

[a] Number of objects for which both of the flux ratios of $C_{IV}\lambda1549/He_{II}\lambda1640$ and $C_{III}]\lambda1909/C_{IV}\lambda1549$ were measured. Objects with a lower-limit or upper-limit data are not included.

effect of dust extinction on our analysis and discussion is not important.

As clearly shown in Fig. 2a, there is no significant difference in these two flux ratios between the high-z QSO2 sample and the local Sy2 sample. Some HzRGs show similar flux ratios to QSO2s and Sy2s, although other HzRGs show lower $C_{IV}\lambda1549/He_{II}\lambda1640$ and higher $C_{III}]\lambda1909/C_{IV}\lambda1549$ than QSO2s and Sy2s. The logarithmically averaged ratios for these three populations (excluding upper-limits and lower-limits) are summarized in Table 3. These averaged flux ratios are also plotted in Fig. 2b. The average flux ratios of HzRGs appears systematically different to those of QSO2s and Sy2s. To see the statistical significance of the differences in the line flux ratios between HzRGs and QSO2s – Sy2s, the
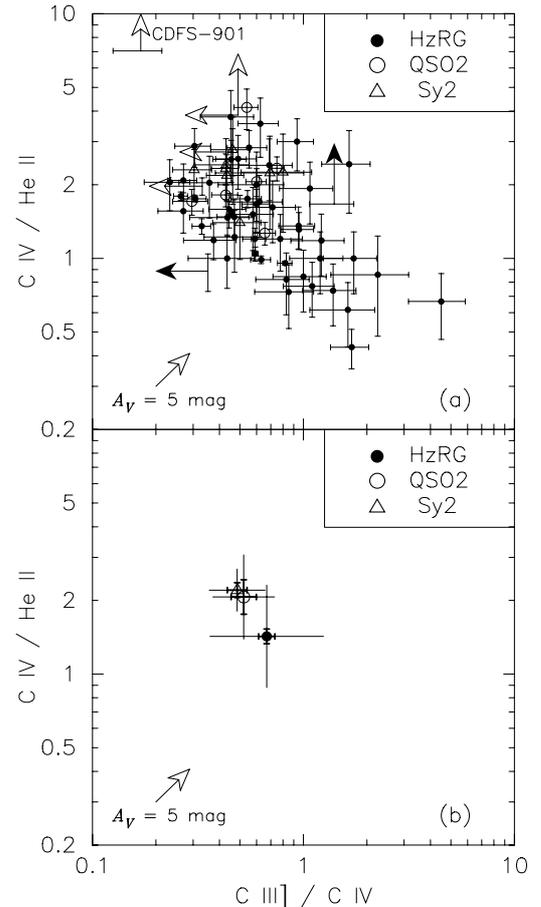

Fig. 2. a) Compiled data plotted on a diagram of $C_{IV}\lambda1549/He_{II}\lambda1640$ versus $N_V\lambda1240/C_{IV}\lambda1549$. Arrows denote the upper-limit or lower-limit on the flux ratios. Filled circles and arrows denote the HzRG data and open circles and arrows denote the QSO2 data. Open triangles denote the Sy2 data. The arrow at the lower-left corner in the panel denote the effect of a correction for dust extinction ($A_V = 5$ mag). **b)** Logarithmically averaged flux ratios of HzRGs (filled circle), QSO2s (open circle) and Sy2s (open triangle) plotted on a diagram of $C_{IV}\lambda1549/He_{II}\lambda1640$ versus $N_V\lambda1240/C_{IV}\lambda1549$. The arrow at the lower-left corner is the same as in **a)**. Thin bars denote the RMS of the data distribution, and thick bars denote the estimated errors on the averaged values.

Kolmogorov-Smirnov (K-S) statistical test is applied to the data, discarding upper limits and lower limits. The null hypothesis is that the flux ratios ($C_{IV}\lambda1549/He_{II}\lambda1640$ and $C_{III}]\lambda1909/C_{IV}\lambda1549$) of HzRGs ($N_{data} = 49$) and QSO2s – Sy2s ($N_{data} = 14$) come from the same underlying population. The derived K-S probabilities are 4.0×10^{-3} for $C_{IV}\lambda1549/He_{II}\lambda1640$ and 8.0×10^{-2} for $C_{III}]\lambda1909/C_{IV}\lambda1549$. These results suggest that the difference in the $C_{IV}\lambda1549/He_{II}\lambda1640$ ratio is statistically significant while the difference in the $C_{III}]\lambda1909/C_{IV}\lambda1549$ ratio is statistically marginal.

When focusing only on HzRGs, an anti-correlation between the emission-line flux ratios of $C_{IV}\lambda1549/He_{II}\lambda1640$ and $C_{III}]\lambda1909/C_{IV}\lambda1549$ is apparent in Fig. 2a. To examine the statistical significance of this correlation, the Spearman rank-order test is applied to the HzRG data, discarding upper limits

and lower limits. The derived Spearman rank-order correlation coefficient (r_S) and their statistical significance $p(r_S)$, which is the probability of the data being consistent with the null hypothesis that the flux ratios are not correlated, are $r_S = -0.53$ and $p(r_S) = 2.5 \times 10^{-4}$ ($N_{\text{data}} = 49$). This indicates that the apparent anti-correlation between $\text{C\,IV}\lambda1549/\text{He\,II}\lambda1640$ and $\text{C\,III}]\lambda1909/\text{C\,IV}\lambda1549$ of HzRGs is statistically significant. This significance does not disappear by including QSO2s and Sy2s: the corresponding Spearman rank-order correlation coefficient and its statistical significance become $r_S = -0.46$ and $p(r_S) = 2.8 \times 10^{-4}$ ($N_{\text{data}} = 63$). This anti-correlation has also been shown by Allen et al. (1998) for a smaller HzRG sample. We will discuss the interpretation of this trend in Sect. 4.1.

3. Photoionization models

To provide a quantitative interpretation of Fig. 2, we carried out photoionization model calculations. The method and the results are given below.

3.1. Model method

We performed model runs by using the public photoionization code Cloudy version 94[2] (Ferland 1997; Ferland et al. 1998). For simplicity, we assumed uniform gas density clouds with a plane-parallel geometry, and we examined both dust-free and dusty cases. For the models with dust, Orion-type graphite and silicate grains (Baldwin et al. 1991; Ferland 1997) were included. Note that the calculations are not sensitive to the assumption of the grain composition (Sect. 4.1.2). Effects of dust grains on the depletion of heavy elements and on the radiative transfer were considered by Cloudy. The parameters for the calculations are (1) the spectral energy distribution (SED) of the photoionizing continuum radiation; (2) the hydrogen density of a cloud (n_H); (3) the ionization parameter (U), i.e., the ratio of the ionizing photon density to the hydrogen density at the irradiated surface of a cloud; (4) the column density of a cloud (N_H); and (5) the elemental composition of the gas.

As for the SED of the ionizing photons, two extreme cases of SED were investigated. The first one is a SED with a weak UV thermal bump, which matches the HST QSO templates (Zheng et al. 1998; Telfer et al. 2002; see Marconi et al. 2004 for more details). The second one has a strong UV thermal bump to match the QSO template by Scott et al. (2004). Both SEDs have the same optical to X-ray ratio α_{OX} (Zamorani et al. 1981), i.e., $\alpha_{OX} = -1.49$ (see Elvis et al. 2002), but different slopes in the energy range of $9.1\,\text{eV} \leq h\nu \leq 35.5\,\text{eV}$; $\alpha = -2.17$ for the SED with a strong UV bump and $\alpha = -1.71$ for the SED with a weaker UV bump, where $f_\nu \propto \nu^\alpha$. See Fig. 3 for a graphical representation of the two SEDs. For convenience, in Fig. 3 we also show the SED deduced by Mathews & Ferland (1983) that has been sometimes used for photoionization model calculations (see Ferland 1997), although we do not use this SED in this work.
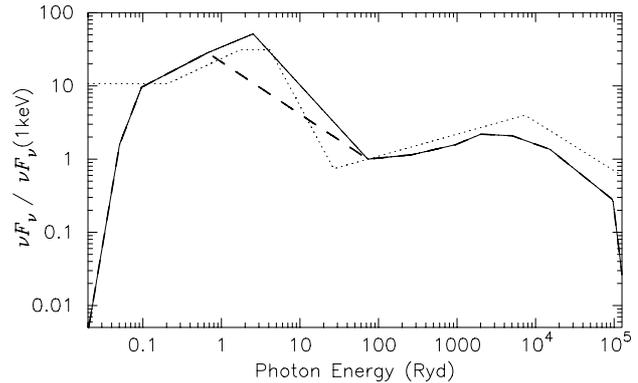
---

[2] We confirmed for some models that the results of the calculations do not change significantly if using Cloudy version 96 instead of version 94; the difference is ~10% at maximum.

**Fig. 3.** Adopted SEDs for our photoionization model calculations. Thin solid line denotes a SED with a strong UV bump and thick dashed line denotes a SED with a weak UV bump. Thin dotted line denotes the SED used by Mathews & Ferland (1983). All the three SEDs are normalized to the flux at 1 keV ($\simeq 73$ Ryd).

We investigated gas clouds with gas densities $n_H = 10^2\,\text{cm}^{-3}$, $10^3\,\text{cm}^{-3}$, $10^5\,\text{cm}^{-3}$ and $10^6\,\text{cm}^{-3}$, and ionization parameters $U = 10^{-2.8}-10^{-0.8}$, as presented in Sect. 3.2. The column density N_H was determined by the criterion that the calculations for dust-free gas clouds were stopped when the temperature falls to 100 K, below which the gas does not contribute significantly to the observed optical emission line spectra. Although this lower-limit temperature is much lower than other calculations for ionization-bounded clouds in the literature, this criterion is necessary to calculate low-density dust-free gas clouds with a high metallicity because the equilibrium temperature of such gas clouds is sometimes lower than 1000 K, as it will be shown later (see also Ferland et al. 1984). For models with dust grains, the stopping temperature was set to 2000 K. This is because the gas temperature does not decrease efficiently in partially-ionized regions when clouds contain dust, due mainly to the depletion of heavy elements (i.e., coolants) and to the heating by photoelectrons emitted from grains (see, e.g., Shields & Kennicutt 1995 for details). Note that the results of our calculations are not sensitive to the lower-limit temperature because we are concerned only with relatively high-ionization emission lines, which arise in fully-ionized regions, and not within partially-ionized regions. For the chemical composition of dust-free gas clouds, we assumed that the all metals scale by keeping solar proportions except for nitrogen, that scales as the square power of other metal abundances, because nitrogen is a secondary element (see, e.g., Hamann et al. 2002). Here the solar elemental abundances are taken from Grevesse & Anders (1989) with extensions by Grevesse & Noels (1993). For dusty gas clouds, we assumed the depleted gas-phase elemental abundance ratios by adopting the depletion factors given by Ferland (1997).

3.2. Model results

In Figs. 4–6, the results of the model calculations are plotted on a diagram with $\text{C\,IV}\lambda1549/\text{He\,II}\lambda1640$ and $\text{C\,III}]\lambda1909/\text{C\,IV}\lambda1549$, for both dust-free and dusty cases. Models for low-density gas clouds ($n_H = 10^2\,\text{cm}^{-3}$ and
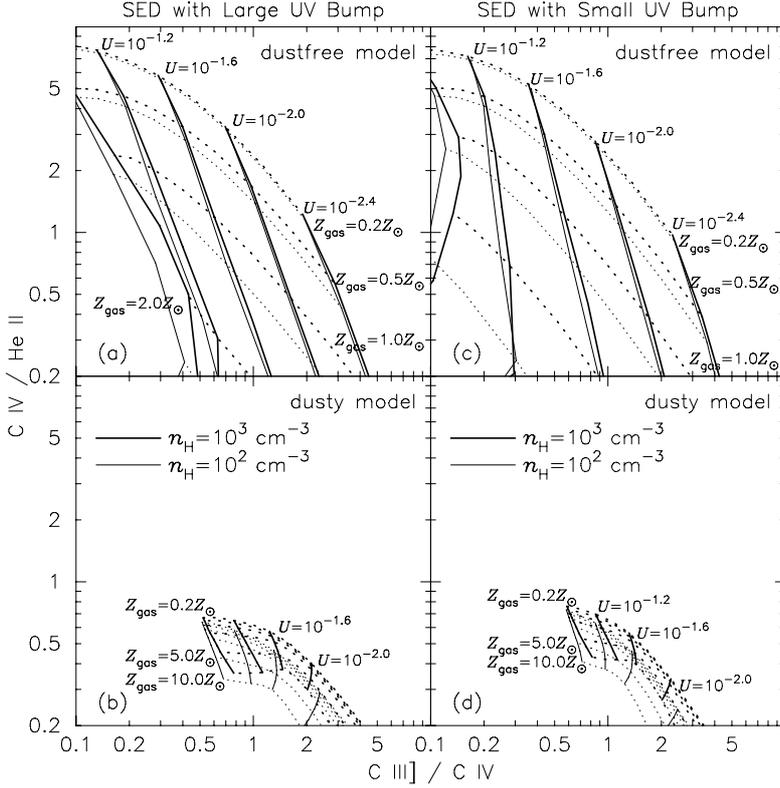
Fig. 4. Model results plotted on a diagram of CIVλ1549/HeIIλ1640 versus CIII]λ1909/CIVλ1549. Models for gas clouds with $n_{\rm H} = 10^2$ cm^{-3} (thin lines) and 10^3 cm^{-3} (thick lines) are presented. Constant-$Z_{\rm gas}$ sequences and constant-U sequences are denoted by dotted and solid lines, respectively. **a)** Dust-free models adopting the input SED with a large 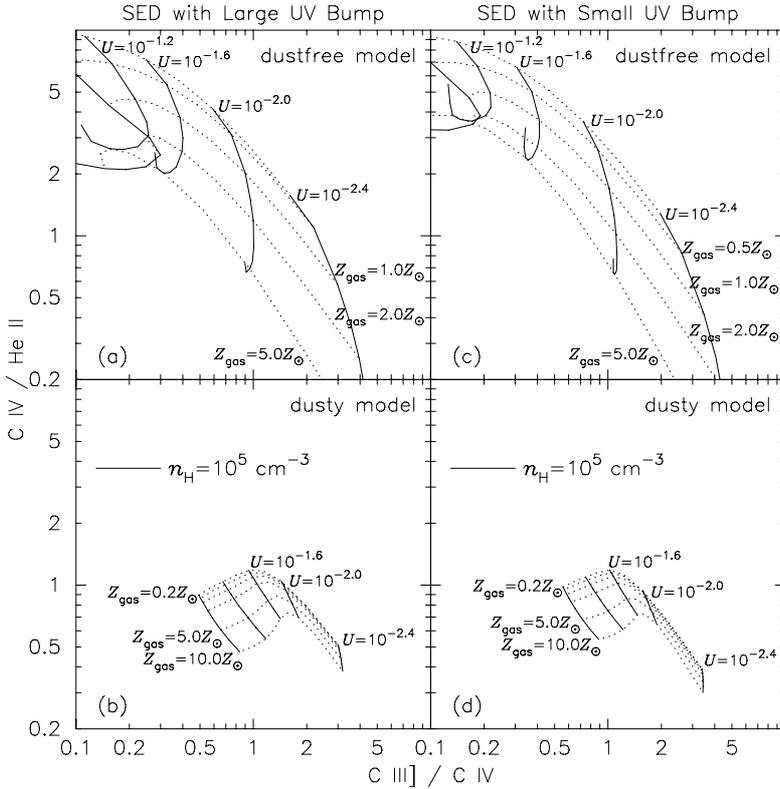UV bump. **b)** Dusty models adopting the input SED with a large UV bump. **c)** Dust-free models adopting the input SED with a small UV bump. **d)** Dusty models adopting the input SED with a small UV bump.

Fig. 5. Same as Fig. 4 but models with $n_{\rm H} = 10^5$ cm^{-3} are plotted. In panels **a)** and **c)**, constant-$Z_{\rm gas}$ sequences (dotted lines) are plotted for $Z_{\rm gas} = 0.2, 0.5, 1.0, 2.0$ and $5.0 \, Z_\odot$ (but not for $Z_{\rm gas} = 10.0 \, Z_\odot$), although constant-$U$ sequences (solid lines) are plotted for the range $0.2 \leq Z_{\rm gas}/Z_\odot < 10.0$.

10^3 cm^{-3}) are presented in Fig. 4, those for high-density gas clouds ($n_{\rm H} = 10^5$ cm^{-3}) are presented in Fig. 5, and those for very high-density gas clouds ($n_{\rm H} = 10^6$ cm^{-3}) are presented in Fig. 6. For low-density cases, the difference of the model results between those with $n_{\rm H} = 10^2$ cm^{-3} and those with $n_{\rm H} = 10^3$ cm^{-3} is very small.

For low-density gas clouds without dust grains, the flux ratio of CIVλ1549/HeIIλ1640 strongly depends on the gas metallicity while CIII]λ1909/CIVλ1549 allows to remove the degeneracy with U, and thus the diagram with CIVλ1549/HeIIλ1640 and CIII]λ1909/CIVλ1549 is good metallicity diagnostic (Figs. 4a and 4c). The strong variation of CIVλ1549/HeIIλ1640
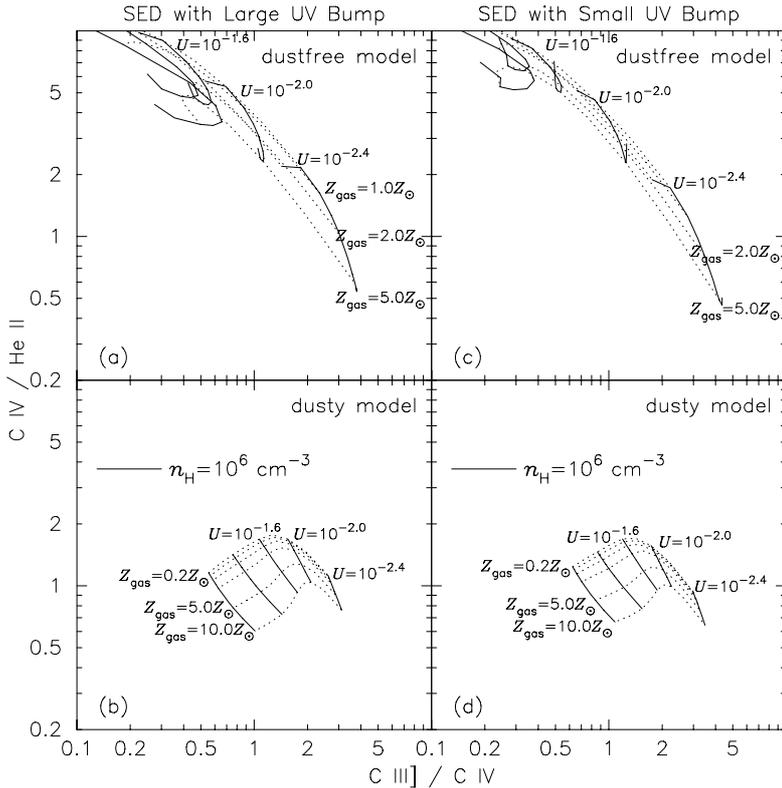
Fig. 6. Same as Fig. 5 but models with $n_H = 10^6$ cm^{-3}.

with metallicity is due to the strong dependence of C IVλ1549 emissivity on the gas temperature, which decreases rapidly with metallicity (in dust-free clouds) due to an efficient cooling by infrared fine-structure lines (e.g., Ferland et al. 1984). The metallicity dependencies of some infrared fine-structure lines ([O III]88 μm, [N III]57 μm and [Ne III]15.6 μm) and gas temperature for gas clouds with $n_H = 10^2$ cm^{-3} are shown in Fig. 7. Here we adopt the averaged temperature over doubly-ionized helium regions as a representative temperature in photoionization equilibrium. The fluxes of the fine-structure lines plotted in Fig. 7 are normalized to the Hβ flux, because the Hβ flux scales with the ionization photon flux.

The metallicity dependence of C IVλ1549/He IIλ1640 in dust-free gas clouds becomes weaker at higher gas densities (Figs. 5a, 5c, 6a, and 6c). This is mainly due to the decreased cooling efficiency of infrared fine-structure lines, which are suppressed in high-density gas clouds owing to collisional de-excitation (Fig. 7). However, even when gas clouds with $n_H = 10^5$ cm^{-3} are concerned, the diagram with C IVλ1549/He IIλ1640 and C III]λ1909/C IVλ1549 maybe useful to constrain the gas metallicity, because the C IVλ1549/He IIλ1640 ratio depends on metallicity even at $n_H = 10^5$ cm^{-3}, although the inferred metallicity is different depending on the specific gas density (Figs. 5a and 5c). The C IVλ1549/He IIλ1640 versus C III]λ1909/C IVλ1549 diagram is no more useful when the gas density is very high, $n_H = 10^6$ cm^{-3} (Figs. 6a and 6c). The metallicity dependence of the C IVλ1549/He IIλ1640 has almost disappeared at this gas density. However, as shown later, the very high-density models ($n_H = 10^6$ cm^{-3}) do not provide a good description of the observed data.

Gas clouds with dust grains show only a very weak dependence of C IVλ1549/He IIλ1640 on metallicity (Figs. 4b, 4d, 5b, 6d, 6b, and 6d). This is mainly because the equilibrium temperature of gas clouds does not drop off significantly when gas metallicity is high, thanks to the presence of dust grains (Fig. 7d; see Shields & Kennicutt 1995 for more details). This result is almost independent of the adopted SED, gas density and ionization parameter.

Figures 4–6 indicate that the results with a large UV bump SED and with a small UV bump SED are similar. We thus conclude that SED effects on our analysis and discussion are negligible. In the following discussion, we only refer to the models with a small UV bump SED.

Note that the diagnostic diagram on which we are focusing has been investigated for various purposes in the past, since all the three lines (He IIλ1640, C IVλ1549 and C III]λ1909) are very strong and the wavelength separation is small (i.e., their ratios are little sensitive to dust extinction). Allen et al. (1998) investigated photoionization models and fast-shock models showing that the data of HzRGs on the C IVλ1549/He IIλ1640 versus C III]λ1909/C IVλ1549 diagram are consistent with photoionization, but are hard to account with by fast-shock models. Groves et al. (2004b) showed that this diagram is useful to examine the gas metallicity of NLRs and mentioned that HzRGs may have gas clouds with sub-solar metallicity. We use this diagram to analyze the gas metallicity of NLRs for a larger sample of high-z narrow-line AGNs and to investigate the possible metallicity evolution of NLRs.

Finally we tackle the issue of whether the flux of C III]λ1909 is significantly contaminated by the Si III]$\lambda\lambda$1883,1892 emission. The predicted ratio of
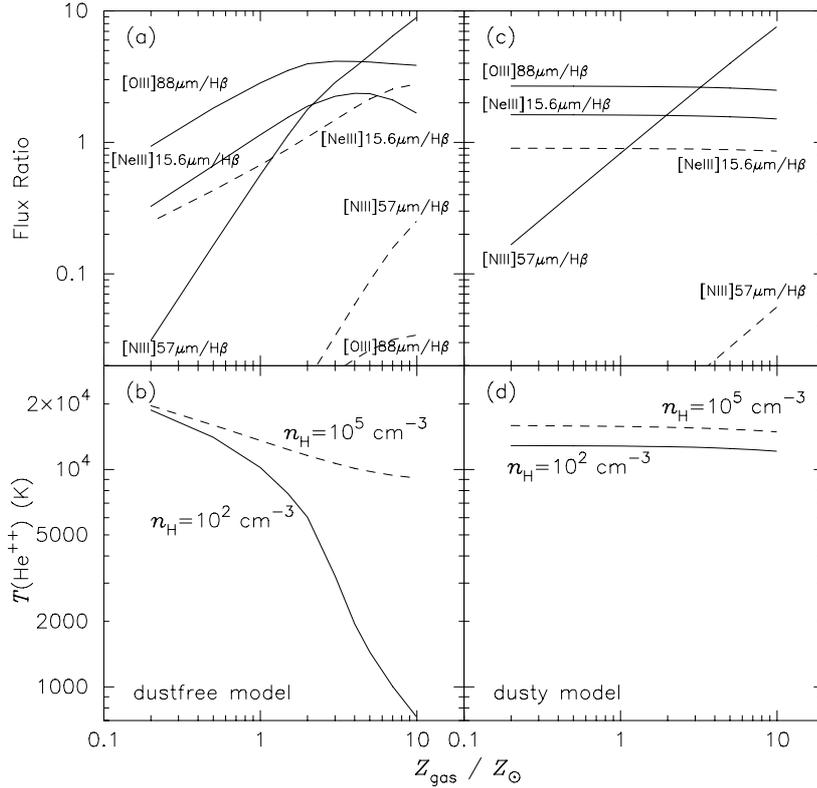
Fig. 7. a) Predicted flux ratios of [O$_{\rm III}$]88 μm/Hβ, [N$_{\rm III}$]57 μm/Hβ and [Ne$_{\rm III}$]15.6 μm/Hβ as functions of metallicity, from dust-free gas clouds with $n_{\rm H} = 10^2$ cm^{-3} (solid lines) and those with $n_{\rm H} = 10^5$ cm^{-3} (dashed lines). The ionization parameter of $U = 10^{-2.0}$ and the input SED with a small UV bump are assumed. **b)** Averaged temperature of doubly-ionized helium regions of dust-free gas clouds with $n_{\rm H} = 10^2$ cm^{-3} (solid line) and those with $n_{\rm H} = 10^5$ cm^{-3} (dashed line) as a function of metallicity. The ionization parameter and the adopted SED are the same as **a)**. **c)** Same as **a)** but for clouds with dust grains. The predicted flux ratio of [O$_{\rm III}$]88 μm/Hβ is too low (<0.01) and thus not presented in the panel. **d)** Same as **b)** but for clouds with dust grains.

Si$_{\rm III}$]$\lambda\lambda$1883,1892/C$_{\rm III}$]λ1909 is plotted as a function of ionization parameter in Fig. 8. Here we investigate gas clouds with $(n_{\rm H}, Z_{\rm gas}) = (10^2$ cm^{-3}, 0.5 $Z_\odot$), $(10^2$ cm^{-3}, 2.0 $Z_\odot$), $(10^5$ cm^{-3}, 0.5 $Z_\odot$) and $(10^5$ cm^{-3}, 2.0 $Z_\odot$). For clouds with dust grains, the predicted ratio is ∼0.01 regardless of density, metallicity and ionization parameter. The contribution of Si$_{\rm III}$]$\lambda\lambda$1883,1892 is thus negligible when dusty clouds are concerned. For dust-free clouds, the predicted ratios are higher, i.e., ∼0.1. However, this is still significantly smaller than the measurement errors on C$_{\rm III}$]λ1909 fluxes. Therefore, we conclude that the contribution of Si$_{\rm III}$]$\lambda\lambda$1883,1892 does not affect our results and discussion significantly.

4. Discussion

4.1. Comparison of the data with models

4.1.1. Shock models

Before comparing the data presented in Sect. 2 with the photoionization models presented in Sect. 3, we examine whether shock models can explain the observed flux ratios. In Fig. 9, we compare the data of the HzRG, QSO2 and Sy2 samples with the shock models presented by Dopita & Sutherland (1996). Both pure shock-only models and shock-plus-precursor models are examined here, with the parameter ranges of the shock velocity 150 km s^{-1} ≤ $v_{\rm shock}$ ≤ 500 km s^{-1} and the magnetic parameter 0 μG cm$^{-3/2}$ ≤ $B/n^{1/2}$ ≤ 4 μG cm$^{-3/2}$. As shown in Fig. 9, both pure shock-only models and shock-plus-precursor models underpredict the flux ratio of C$_{\rm III}$]λ1909/C$_{\rm IV}\lambda$1549 and thus cannot explain the observed data. This suggests that the main ionization mechanism of NLRs (or at least the C$_{\rm IV}\lambda$1549,
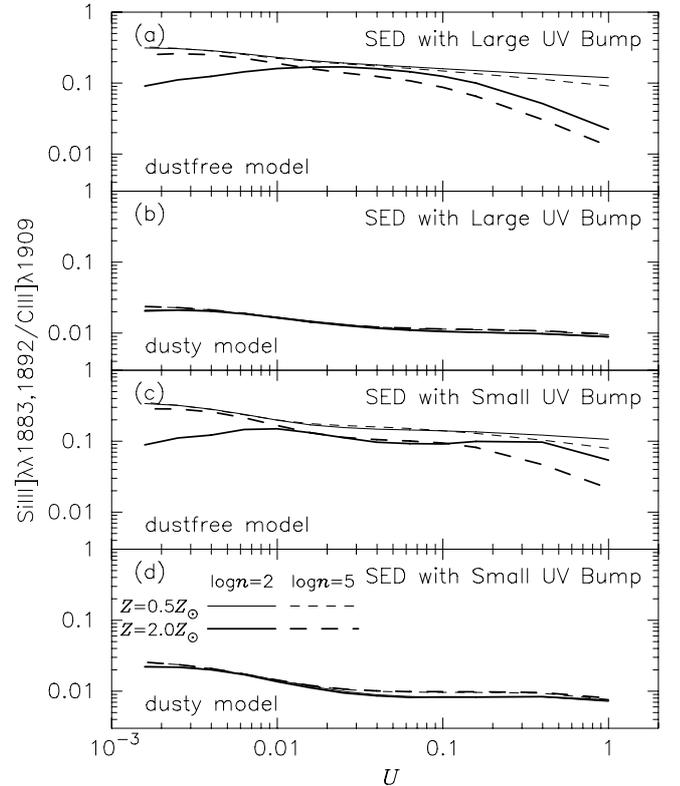

Fig. 8. Predicted flux ratio of Si$_{\rm III}$]$\lambda\lambda$1883,1892/C$_{\rm III}$]λ1909 as a function of ionization parameter. Solid and dashed lines denote the models with $n_{\rm H} = 10^2$ cm^{-3} and $n_{\rm H} = 10^5$ cm^{-3}, respectively. Thin and thick lines denote the models with $Z_{\rm gas} = 0.5$ $Z_\odot$ and $Z_{\rm gas} = 2.0$ $Z_\odot$, respectively. **a)** Dust-free models with a large UV bump SED. **b)** Dusty models with a large UV bump SED. **c)** Dust-free models with a small UV bump SED. **d)** Dusty models with a small UV bump SED.
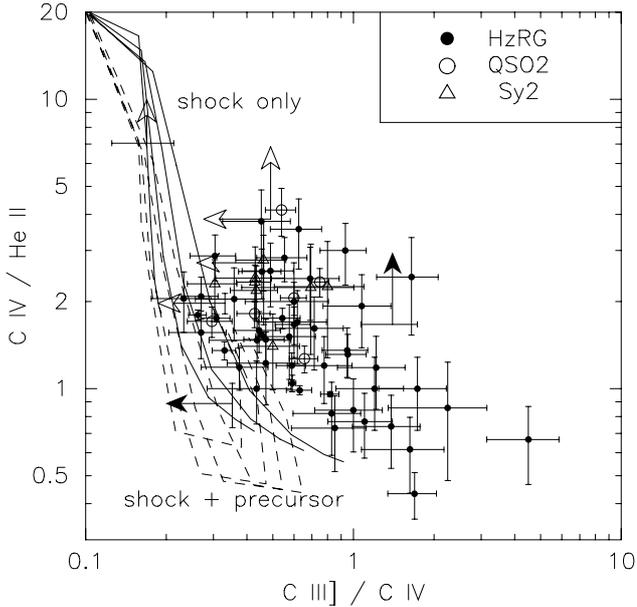
Fig. 9. Same as Fig. 2a but shock models of Dopita & Sutherland (1996) are overplotted. Solid and dashed lines denote the predictions of the pure shock-only models and the shock-plus-precursor models, respectively, with magnetic parameters of 0, 1, 2, and 4 μG cm$^{-3/2}$ (from left to right in the panel). Shock models with faster shock velocities are located at lower positions in the panel.

HeIIλ1640 and CIII]λ1909 emitting regions in NLRs) is not associated with shocks, but rather is due to photoionization. Figure 9 also suggests that the difference in the flux ratios between HzRGs and QSO2s – Sy2s cannot be ascribed to shocks. Instead, a preferential contribution of shocks to QSO2s (not to HzRGs) is required if shocks are at the origin of the difference in the flux ratios. This requirement is in the opposite direction as the natural expectation (HzRGs should be more affected by shocks because of jets and expanding radio lobes). Therefore, the systematic difference in the flux ratios between HzRGs and QSO2s – Sy2s must be ascribed to causes other than shocks. This issue will be discussed further in Sect. 4.1.3.

4.1.2. Dust grains

In Fig. 10, we compare the observational data with the results of our photoionization model calculations, both with and without dust grains. Contrary to the dust-free models, the dusty models predict too narrow ranges of the CIVλ1549/HeIIλ1640 flux ratio, regardless of the gas density (Figs. 10b, 10d, and 10f). The CIVλ1549/HeIIλ1640 flux ratio varies only by a factor of 3 at maximum even when the metallicity varies in the range $0.2 \leq Z_{gas}/Z_{\odot} \leq 10.0$. More importantly, the dusty models cannot explain values of CIVλ1549/HeIIλ1640 larger than ~1.5, which are instead observed in most sources. These results suggest that the CIVλ1549, HeIIλ1640 and CIII]λ1909 emitting regions in NLRs are dust-free. This is consistent with previous works in that gas clouds in the high-ionization part of NLRs are dust-free (e.g., Marconi et al. 1994; Ferguson et al. 1997; Nagao et al. 2003). We verified that the effects of changing the grain composition (see Ferland 1997 for details) are

less than 30% for the line flux ratios. We thus conclude that the models with dust grains are not appropriate to interpret the ratios of CIVλ1549/HeIIλ1640 and CIII]λ1909/CIVλ1549.

Groves et al. (2004b) reported that the rest-UV emission-line spectra of HzRGs are well described by their dusty, radiation pressure dominated photoionization models (Dopita et al. 2002; Groves et al. 2004a), which appears to be in contrast to our conclusion. However the results of the dusty photoionization models presented here are roughly consistent with those reported by Groves et al. (2004b) and there are likely slight differences due to the different depletion factors adopted for the model calculations. The most important result of dusty photoionization models (both presented by us and by Groves et al. 2004b) is that the dusty models cannot explain the several observational data points with CIVλ1549/HeIIλ1640 > 1.5. Although such observational data were rather rare in the presentation by Groves et al. (2004b), our data compilation clarifies that the HzRGs with the flux ratio of CIVλ1549/HeIIλ1640 larger than 1.5 are not rare objects but rather are quite common (Fig. 2a).

4.1.3. Ionization parameter

In the case of dust-free models, the models with low density ($n_{\rm H}$ = 10^2 cm^{-3} and 10^3 cm^{-3}) and high density ($n_{\rm H}$ = 10^5 cm^{-3}) can successfully explain the observed range of flux ratios CIVλ1549/HeIIλ1640 and CIII]λ1909/CIVλ1549 (Figs. 10a and 10c), while the very high-density models ($n_{\rm H}$ = 10^6 cm^{-3}) cannot explain most of the observational data (Fig. 10e). We can deduce that $n_{\rm H}$ = 10^6 cm^{-3} is an upper bound to the average NLR density. Both high-density models and low-density models suggest that the observational data are consistent with clouds with an ionization parameter $10^{-2.2} \lesssim U \lesssim 10^{-1.4}$ for HzRGs and $U \approx 10^{-1.6}$ for QSO2s and Sy2s (Figs. 10a and 10c). The model sequences with a constant ionization parameter have negative slope in the diagram of CIVλ1549/HeIIλ1640 versus CIII]λ1909/CIVλ1549, which is consistent with the observational trend described in Sect. 2.2. Therefore the anti-correlation between CIVλ1549/HeIIλ1640 and CIII]λ1909/CIVλ1549 seen in HzRGs can be naturally explained by the wide range of the ionization parameter for HzRGs. Although the inferred range of ionization parameter is higher than the range estimated through rest-frame optical diagnostics (which use lower ionization emission lines) reported by some previous works (e.g., Ferland & Netzer 1983; Ho et al. 1993), it is consistent with previous estimates of the ionization parameter for the high-ionization parts in NLRs (e.g., Oliva et al. 1994; Murayama & Taniguchi 1998; Nagao et al. 2001a, 2001b).

4.1.4. Gas density and metallicity

As mentioned in the last subsection, photoionization models with $n_{\rm H}$ = 10^6 cm^{-3} predict too narrow ranges of the flux ratios of CIVλ1549/HeIIλ1640 and CIII]λ1909/CIVλ1549 with respect to the observed ranges. This suggests that the typical density of the CIVλ1549, HeIIλ1640 and CIII]λ1909-emitting
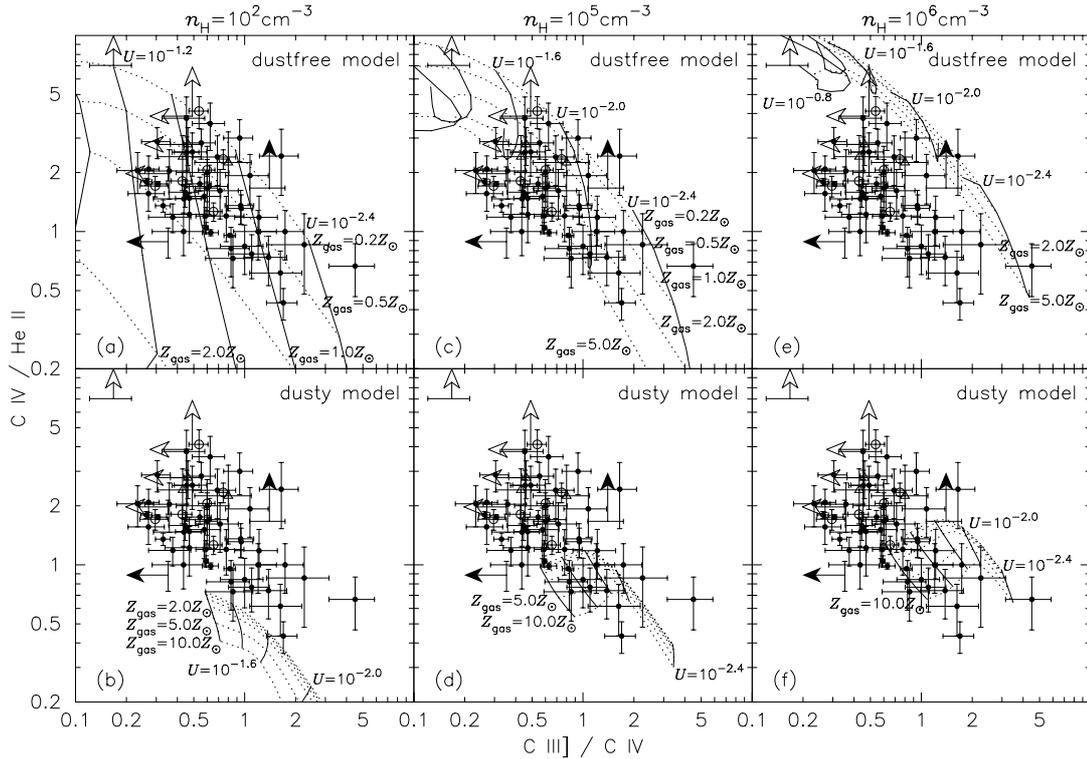
Fig. 10. Observational data and model results are plotted on a diagram of $CIV\lambda1549/HeII\lambda1640$ versus $CIII]\lambda1909/CIV\lambda1549$. A SED with a small UV bump is adopted in the models. Symbols are the same as those in Fig. 2. Dust-free models are plotted in the upper panels (**a**), **c**), **e**)) while dusty models are plotted in the lower panels (**b**), **d**), **f**)). Adopted gas densities are $n_H = 10^2$ cm^{-3} (panels **a**), **b**)), $n_H = 10^5$ cm^{-3} (panels **c**), **d**)), and $n_H = 10^6$ cm^{-3} (panels **e**), **f**)).

region in the NLR should be less than 10^6 cm^{-3}. Therefore, in the following discussion, we consider only the two models, i.e., the low-density models with $n_H = 10^2$ cm^{-3} (note that the results are very similar if adopting $n_H = 10^3$ cm^{-3}) and the high-density models with $n_H = 10^5$ cm^{-3}.

As shown in Figs. 10a and 10c, the estimated metallicity is different when different gas densities are adopted. Models with $n_H = 10^2$ cm^{-3} suggest sub-solar metallicities ($0.2 \lesssim Z_{gas}/Z_\odot \lesssim 1.0$; Fig. 10a) while models with $n_H = 10^5$ cm^{-3} suggest a wide metallicity range ($0.2 \lesssim Z_{gas}/Z_\odot \lesssim 5.0$; Fig. 10c). The "low-density and sub-solar metallicity" scenario appears to be consistent with the results reported by Iwamuro et al. (2003), while the "high-density with wide metallicity distribution" scenario appears in agreement with the results reported by De Breuck et al. (2000). Although some observational data with lower $CIV\lambda1549/HeII\lambda1640$ and $CIII]\lambda1909/CIV\lambda1549$ ratios appear to deviate from the model predictions with $n_H = 10^5$ cm^{-3} (Fig. 10c), these deviations can be reconciled by introducing a moderate amount of extinction. Although the above two scenarios are hard to discriminate only by means of the $CIV\lambda1549/HeII\lambda1640$ versus $CIII]\lambda1909/CIV\lambda1549$ diagram, the actual situation may be intermediate between the two possible scenarios (Sect. 4.2). Note that the absolute values of the inferred gas metallicity are not very accurate due to a density dependence of the flux ratio $CIV\lambda1549/HeII\lambda1640$ at high-densities ($n_H \gtrsim 10^4$ cm^{-3}). Nevertheless the diagnostic diagram in Fig. 10 is useful if we are interested in the relative metallicity trends of NLR clouds, or in the evolution of gas metallicity,

adopting the assumption that there are no strong correlations between gas density and redshift. Finally, we note that the density affects the inferred metallicity mostly at $Z_{gas} \gtrsim 0.5 Z_\odot$. At low metallicities ($Z_{gas} \sim 0.2 Z_\odot$) the models are less sensitive to the gas density (Figs. 10a and 10c). This result is important since it allows to use this diagnostic diagram to identify low metallicity NLRs, regardless of the gas density.

4.2. Comparison with the $N V \lambda 1240$ diagnostics

The gas metallicity of the BLR clouds in QSOs has been often investigated by using the diagnostic flux ratios of $NV\lambda1240/CIV\lambda1549$ and $NV\lambda1240/HeII\lambda1640$ (e.g., Hamann & Ferland 1992, 1999; Dietrich et al. 2003; Nagao et al. 2006). This method has been sometimes applied also to the NLR clouds (e.g., van Ojik et al. 1994; Villar-Martin et al. 1999; De Breuck et al. 2000; Vernet et al. 2001). Therefore it is interesting to compare our diagnostics with the $NV\lambda1240$ diagnostics. In Fig. 11, the observational data are compared with the photoionization models for $n_H = 10^2$ cm^{-3} and $n_H = 10^5$ cm^{-3} on the diagram of $NV\lambda1240/CIV\lambda1549$ versus $CIV\lambda1549/HeII\lambda1640$, and $NV\lambda1240/HeII\lambda1640$ versus $CIV\lambda1549/HeII\lambda1640$. Although high ratios of $NV\lambda1240/CIV\lambda1549$ and $NV\lambda1240/HeII\lambda1640$ are sometimes interpreted simply as a result of high metallicities, the low-density models ($n_H = 10^2$ cm^{-3}) with a high metallicity predict not only high $NV\lambda1240/CIV\lambda1549$ ratios but also very low $CIV\lambda1549/HeII\lambda1640$ ratios, in disagreement
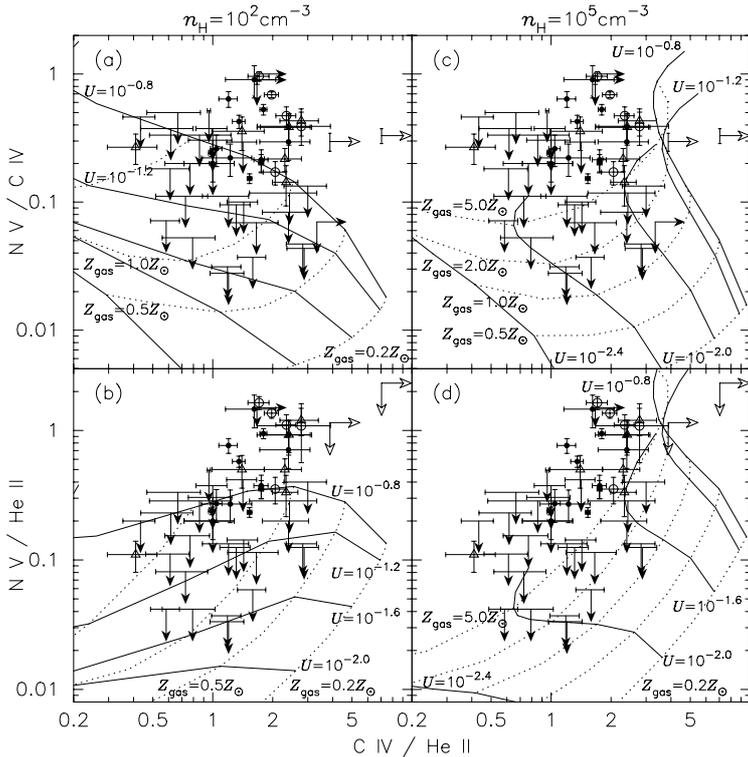
Fig. 11. Observed and predicted flux ratios. Dust-free models with a small UV bump are plotted. Symbols are the same as those in Fig. 2. Observed data compared with models for $n_H = 10^2$ cm^{-3} on a diagram of $N_V\lambda1240/C_{IV}\lambda1549$ versus $C_{IV}\lambda1549/He_{II}\lambda1640$ **a)** and on a diagram of $N_V\lambda1240/He_{II}\lambda1640$ versus $C_{IV}\lambda1549/He_{II}\lambda1640$ **b)**. Data compared with models for $n_H = 10^5$ cm^{-3} on $N_V\lambda1240/C_{IV}\lambda1549$ versus $C_{IV}\lambda1549/He_{II}\lambda1640$ **c)** and on $N_V\lambda1240/He_{II}\lambda1640$ versus $C_{IV}\lambda1549/He_{II}\lambda1640$ **d)**.

with the observed data (Fig. 11a). This is mainly attributed to the decreased equilibrium gas temperature due to the efficient cooling by infrared fine-structure lines as investigated in Sect. 3.2 (Fig. 7). Moreover the low-density models predict $N_V\lambda1240/He_{II}\lambda1640 < 0.4$ when $U \leq 10^{-0.8}$ is concerned, which is also in disagreement with the observed data (Fig. 11b). The high-density models ($n_H = 10^5$ cm^{-3}), on the other hand, predict higher $C_{IV}\lambda1549/He_{II}\lambda1640$ ratios than the low-density models owing to the suppressed cooling. Since the high-density models predict higher $C_{IV}\lambda1549/He_{II}\lambda1640$ ratios than the observed values (Figs. 11c and 11d), the typical gas density of (the high-ionization part of) the NLRs may be lower than $n_H = 10^5$ cm^{-3}.

Although the $N_V\lambda1240$-detected objects appear to have super-solar metallicity, the $N_V\lambda1240$ fluxes of more than half of the objects in the sample are upper-limits and they might be consistent with sub-solar metallicities. Summarizing, since $N_V\lambda1240$ becomes very weak (generally undetected) for $Z_{gas} \lesssim 2 Z_\odot$ NLRs, it is very difficult to investigate the metallicity evolution of the NLR based on the $N_V\lambda1240$ diagnostics.

4.3. Metallicity evolution of the NLRs in AGNs

Now we discuss whether the gas metallicity of the NLRs in high-z AGNs evolves as a function of redshift. We first focus only on the HzRG data, because HzRGs and QSO2s may have different NLR properties, as discussed above. To investigate this issue, we divide the sample of objects having a measurement of both $C_{IV}\lambda1549/He_{II}\lambda1640$ and $C_{III}]\lambda1909/C_{IV}\lambda1549$ (49 objects, discarding the objects with upper-limits or lower-limits) into three groups: $1.2 < z < 2.0$ (17 objects), $2.0 < z < 2.5$ (20 objects) and $2.5 < z < 3.8$ (12 objects). Note

that most of the highest-z sample are at $2.5 < z < 3.0$ and only two objects are at $z > 3$ (Fig. 1a). We calculate the logarithmically averaged flux ratios of $C_{IV}\lambda1549/He_{II}\lambda1640$ and $C_{III}]\lambda1909/C_{IV}\lambda1549$ for these three groups. The results are given in Table 4 and plotted on the diagnostic diagram in Figs. 12a and 12c. The thick errorbars give the estimated errors on the means. As clearly seen, no evolutionary tendency in the flux ratios within our HzRG sample is found. The higher-z objects do not show significant metallicity decrease with respect to the lower-z objects, at variance with the result reported by De Breuck et al. (2000). Although the absolute value of the gas metallicity derived from Fig. 10 is subject to non-negligible uncertainties, as discussed in Sect. 4.1.4, our conclusion is not affected by this issue in terms of relative gas metallicities, i.e., the gas metallicity in NLRs of HzRGs does not change significantly in the redshift range $1.2 < z < 3.8$, or more conservatively, in the range $1.2 < z < 3$ (owing to the lack of objects at $z > 3$).

Recently Nagao et al. (2006) reported that the gas metallicity of the BLR in QSOs with a given luminosity is independent of redshift in the range $2.0 < z < 4.5$. This result is consistent with that obtained for the NLR metallicity of HzRGs presented in this paper. Nagao et al. (2006) also reported that the BLR metallicity is tightly correlated with the QSO luminosity (see also, e.g., Hamann & Ferland 1993, 1999). Motivated by this correlation between BLR metallicity and QSO luminosity, we have investigated whether the NLR metallicity is correlated with the AGN luminosity or not. However, it is very difficult to measure the luminosity of both AGNs and their host galaxies when type-2 AGNs are concerned. This is because the central engine is hidden by the dusty torus and because the broad-band photometric flux is largely attributed to

Table 4. Averaged diagnostic flux ratios of HzRGs.

Sample	Number[a]	C IV / He II	C III] / C IV
HzRG $1.2 < z < 2.0$	17	$1.65^{+0.20}_{-0.18}$	$0.66^{+0.08}_{-0.07}$
HzRG $2.0 < z < 2.5$	20	$1.27^{+0.13}_{-0.11}$	$0.70^{+0.11}_{-0.09}$
HzRG $2.5 < z < 3.8$	12	$1.39^{+0.25}_{-0.21}$	$0.64^{+0.16}_{-0.13}$
HzRG $41.5 < \log L(\text{HeII})^b < 42.5$	13	$1.72^{+0.26}_{-0.23}$	$0.89^{+0.10}_{-0.09}$
HzRG $42.5 < \log L(\text{HeII})^b < 43.0$	21	$1.39^{+0.15}_{-0.13}$	$0.63^{+0.11}_{-0.09}$
HzRG $43.0 < \log L(\text{HeII})^b < 45.0$	15	$1.26^{+0.16}_{-0.14}$	$0.58^{+0.09}_{-0.08}$
HzRG total	49	$1.42^{+0.10}_{-0.09}$	$0.67^{+0.06}_{-0.06}$

[a] Number of objects for which both of the flux ratios of $\text{CIV}\lambda1549/\text{HeII}\lambda1640$ and $\text{CIII}]\lambda1909/\text{CIV}\lambda1549$ were measured. Objects with a lower-limit or upper-limit data are not included.
[b] Line luminosity of $\text{HeII}\lambda1640$ in units of erg s^{-1}, calculated from the line flux given by De Breuck et al. (2000).

the nebular emission, not only to the stellar continuum emission. We thus adopt the $\text{HeII}\lambda1640$ emission-line luminosity [$L(\text{HeII})$] as an indicator of the AGN luminosity. This assumption is based on the fact that the $\text{HeII}\lambda1640$ luminosity is simply proportional to the volume of the doubly-ionized helium region, which scales to the AGN luminosity. We calculate $L(\text{HeII})$ from the $\text{HeII}\lambda1640$ flux by adopting a cosmology with (Ω_{tot}, Ω_{m}, Ω_{Λ}) = (1.0, 0.3, 0.7) and $H_0 = 70 \text{ km s}^{-1} \text{ cm}^{-1} \text{ Mpc}^{-1}$. $L(\text{HeII})$ is not corrected for the slit loss, which may be non-negligible for some cases. To investigate the dependence of the line flux ratios on $L(\text{HeII})$, we divide HzRGs into three groups: $41.5 < \log L(\text{HeII}) < 42.5$ (13 objects), $42.5 < \log L(\text{HeII}) < 43.0$ (21 objects), and $43.0 < \log L(\text{HeII}) < 45.0$ (15 objects), where $L(\text{HeII})$ is in units of erg s^{-1}. The logarithmically averaged flux ratios and the RMS of $\text{CIV}\lambda1549/\text{HeII}\lambda1640$ and $\text{CIII}]\lambda1909/\text{CIV}\lambda1549$ for these three groups are given in Table 4, and are plotted on the diagnostic diagram in Figs. 12b and 12d. The thick errorbars give the errors of the means. As a result, we find a systematic trend in our HzRG sample that the HzRGs with larger $L(\text{HeII})$ (i.e., more luminous AGNs) tend to have lower $\text{CIV}\lambda1549/\text{HeII}\lambda1640$ and $\text{CIII}]\lambda1909/\text{CIV}\lambda1549$ flux ratios. This result is consistent with the interpretation that the NLR in more luminous HzRGs have higher metallicity gas clouds. This "luminosity-metallicity relation" for the NLR in HzRGs is in agreement with the same relation seen for the BLRs in high-z QSOs.

Unfortunately the QSO2 sample contains only 6 usable objects and thus it is very difficult to discuss the possible dependences of the NLR metallicity of the QSO2s on redshift and luminosity, at variance with the HzRGs. However it is interesting to search for any possible hints of such dependences based on currently available data. We therefore divide the QSO sample into two groups; one is "lower-z, less-luminous QSO2s" that contains CDFS-153 [$z = 1.536$, $\log L(\text{HeII}) = 41.0$], CDFS-531 [$z = 1.544$, $\log L(\text{HeII}) = 41.4$] and CDFS-027 [$z = 1.603$, $\log L(\text{HeII}) = 41.4$], and the other is "higher-z, more-luminous QSO2s" that contains CDFS-057 [$z = 2.562$, $\log L(\text{HeII}) = 41.6$], CDFS-112a [$z = 2.940$, $\log L(\text{HeII}) = 41.8$] and CXO52 [$z = 3.288$, $\log L(\text{HeII}) = 42.2$], where $L(\text{HeII})$ is again in units of erg s^{-1}. We then calculate the mean flux ratios of $\text{CIV}\lambda1549/\text{HeII}\lambda1640$ and $\text{CIII}]\lambda1909/\text{CIV}\lambda1549$ and their estimated errors for the two groups, which results in

$\text{CIV}\lambda1549/\text{HeII}\lambda1640 = 2.11^{+0.88}_{-0.62}$ and $\text{CIII}]\lambda1909/\text{CIV}\lambda1549 = 0.53^{+0.07}_{-0.06}$ for the former group and $\text{CIV}\lambda1549/\text{HeII}\lambda1640 = 2.02^{+0.19}_{-0.18}$ and $\text{CIII}]\lambda1909/\text{CIV}\lambda1549 = 0.51^{+0.16}_{-0.12}$ for the latter group, respectively. This result suggests that there is no apparent metallicity dependence on redshift and luminosity, although the statistics are extremely poor. Further spectroscopic observations of QSO2s at high-redshift are required to investigate this issue.

It has been observationally confirmed that QSOs including radio galaxies tend to reside in massive elliptical galaxies at least in the local universe (e.g., McLure et al. 1999; Dunlop et al. 2003; Floyd et al. 2004) and probably also in the high-z universe (e.g., Falomo et al. 2005; Kuhlbrodt et al. 2005). Our results suggest that the main star-formation event in such massive host galaxies is completed. This picture is consistent with the recent findings of massive evolved galaxies at $z > 1.5$ (e.g., Cimatti et al. 2004; McCarthy et al. 2004; Labbé et al. 2005; Saracco et al. 2005). The non-evolution of the gas metallicity of the NLR in our sample suggests that the epoch of major chemical enrichment in the host galaxies of QSO2s and HzRGs must have occurred at $z \gtrsim 3$. If the minimum timescale for significant enrichment of carbon (~ 0.5 Gyr) is taken into account, the major epoch of star formation may be at $z \gtrsim 4$.

Finally we briefly discuss a specific, interesting QSO2, CDFS-901 (Fig. 2a). Although the emission-line spectrum of this object is hard to explain by photoionization models, as seen in Fig. 10, it appears to be consistent with pure shock-only models and with shock-plus-precursor models as shown in Fig. 9. This may suggest that the NLR of CDFS-901 is dominated by shocks. However, there is another possibility, that is CDFS-901 may be a narrow-line type-1 QSO, i.e., a brighter analogue of narrow-line Seyfert 1 galaxies (NLS1s). If the emission-line spectrum of CDFS-901 is not from its NLR but from its BLR, its very large $\text{CIV}\lambda1549/\text{HeII}\lambda1640$ ratio (>7.0) is naturally explained, since this flux ratio is expected to be ~ 10 for BLRs (although its $\text{CIII}]\lambda1909/\text{CIV}\lambda1549$ ratio ~ 0.2 is very small for a BLR, e.g., Nagao et al. 2006). Since the X-ray spectral slope (hardness ratio) of this object was not measured due to the lack of photon statistics, its nature remains ambiguous based on the currently available data. This object is interesting because NLS1s are sometimes thought to be AGNs with supermassive black holes in their growing phase (e.g., Mathur 2000).
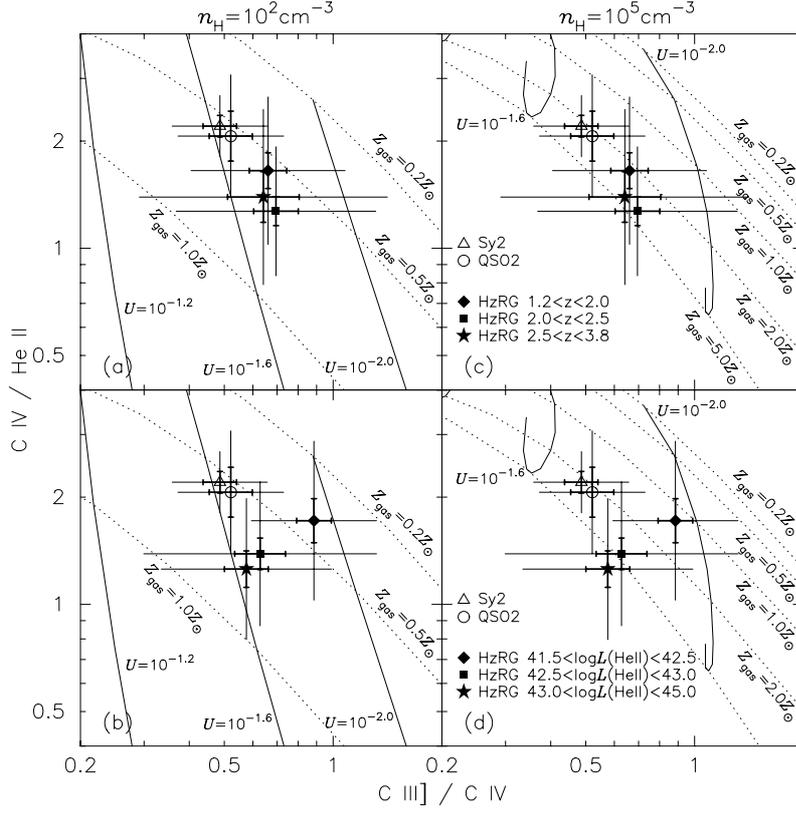
Fig. 12. Averaged flux ratios compared with the model predictions on the CIVλ1549/HeIIλ1640 versus CIII]λ1909/CIVλ1549 diagram. Filled circle, open circle and open triangle denote the average values of the HzRG sample, the QSO2 sample and Sy2s sample. Models with $n_H = 10^2$ cm^{-3} are plotted in panels **a)** and **b)**, while models with $n_H = 10^5$ cm^{-3} are plotted in panels **c)** and **d)**. For both cases, models with a small UV bump SED and without dust are plotted. The redshift dependence of the flux ratios of the HzRGs are investigated in panels **a)** and **c)**, where filled diamond, square and star denote the average flux ratios of the HzRGs at $1.2 < z < 2.0$, $2.0 < z < 2.5$ and $2.5 < z < 3.8$, respectively. The luminosity dependence of the flux ratios of the HzRGs are investigated in panels **b)** and **d)**, where filled diamond, square and star denote the averaged flux ratios of the HzRGs with $41.5 < \log L(\text{HeII}) < 42.5$, $42.5 < \log L(\text{HeII}) < 43.0$, and $43.0 < \log L(\text{HeII}) < 45.0$ respectively, where $L(\text{HeII})$ is in units of erg s^{-1}. Error bars are as in Fig. 2b.

If this object is a high-z analogue of NLS1s, it may be a very interesting target to investigate the evolution of AGN activities and supermassive black holes.

5. Summary

In order to investigate the possible metallicity evolution of NLR gas clouds in AGNs, we compiled the fluxes of CIVλ1549, HeIIλ1640 and CIII]λ1909 for a large sample of narrow-line AGNs, including HzRGs, high-z QSO2s, and local Sy2s. Since all of these three emission lines are moderately strong even in the faint HzRGs and QSO2s, this approach enables us to investigate a large number of such objects. By comparing the compiled flux ratios with the results of our photoionization model calculations, we found the following results.

– The observational data are inconsistent with the predictions of shock models, suggesting that the NLRs are mainly photoionized.
– The photoionization models with dust grains predict too narrow ranges of flux ratios and are in disagreement with the observed ranges, suggesting that the high-ionization part of NLRs (on which we focused in this work) is dust-free.

– The ionization parameter of (the high-ionization parts of) NLRs is estimated to be $10^{-2.2} \lesssim U \lesssim 10^{-1.4}$ for HzRGs and $U \approx 10^{-1.6}$ for QSO2s and Sy2s.
– The photoionization models with $n_H = 10^6$ cm^{-3} cannot explain the observational data, suggesting that the typical gas density is lower than 10^6 cm^{-3}.
– There are two possible interpretations for the observed data: low-density gas clouds ($n_H \lesssim 10^3$ cm^{-3}) with a sub-solar metallicity ($0.2 \lesssim Z_{gas}/Z_\odot \lesssim 1.0$), or high-density gas clouds ($n_H \sim 10^5$ cm^{-3}) with a wide range of gas metallicity ($0.2 \lesssim Z_{gas}/Z_\odot \lesssim 5.0$).
– Our method using only the flux ratios of CIVλ1549/HeIIλ1640 and CIII]λ1909/CIVλ1549 is particularly useful to examine relative difference in gas metallicity of NLR clouds, or to investigate possible metallicity evolution of NLRs, although the inferred absolute values of metallicity contain non-negligible uncertainties.
– Regardless of the density, the proposed diagnostic diagram is useful to identify low metallicity NLRs ($Z_{gas} \sim 0.2 Z_\odot$).
– We find no evidence suggesting a significant evolution of the gas metallicity in the NLRs of HzRGs in the redshift range $1.2 \leq z \leq 3$.

- We find a systematic trend for more luminous AGNs to have more metal-rich NLRs (luminosity-metallicity relation), which is in agreement with the results from the studies on the BLRs.
- The non-evolution of the gas metallicity of the NLRs implies that the major epoch of star formation in the host galaxies is at $z \gtrsim 4$.

References

Allen, M. G., Dopita, M. A., & Tsvetanov, Z. I. 1998, ApJ, 493, 571

Antonucci, R. R. J. 1993, ARA&A, 31, 473

Antonucci, R. R. J., & Miller, J. S. 1985, ApJ, 297, 621

Baldwin, J. A., Ferland, G. J., Martin, P. G., et al. 1991, ApJ, 374, 580

Baldwin, J. A., Hamann, F., Korista, K. T., et al. 2003, ApJ, 583, 649

Baum, S. A., & McCarthy, P. J. 2000, AJ, 119, 2634

Bergeron, J., Maccacaro, T., & Perola, C. 1981, A&A, 97, 94

Cardelli, J. A., Clayton, G. C., & Mathis, J. S. 1989, ApJ, 345, 245

Cimatti, A., Daddi, E., Renzini, A., et al. 2004, Nature, 430, 184

Cohen, M. H., Ogle, P. M., Tran, H. D., Goodrich, R. W., & Miller, J. S. 1999, AJ, 118, 1963

De Breuck, C., Röttgering, H., Miley, G., van Breugel, W., & Best, P. 2000, A&A, 362, 519

De Robertis, M. M., Hutchings, J. B., & Pitts, R. E. 1988, AJ, 95, 1371

Dietrich, M., Hamann, F., Shields, J. C., et al. 2003, ApJ, 589, 722

Dunlop, J. S., McLure, R. J., Kukula, M. J., et al. MNRAS, 340, 1095

Dopita, M. A., Groves, B. A., Sutherland, R. S., Binette, L., & Cecil, G. 2002, ApJ, 572, 753

Dopita, M. A., & Sutherland, R. S. 1996, ApJS, 102, 161

Elvis, M., Risaliti, G., & Zamorani, G. 2002, ApJ, 565, L75

Falomo, R., Kotilainen, J. K., Scarpa, R., & Treves, A. 2005, A&A, 434, 469

Ferguson, J. W., Korista, K. T., & Ferland, G. J. 1997, ApJS, 110, 287

Ferland, G. J. 1997, Hazy: A Brief Introduction to Cloudy 94.00 (Lexington: Univ. Kentucky Dept. Phys. Astron.)

Ferland, G. J., & Netzer, H. 1983, ApJ, 264, 105

Ferland, G. J., Williams, R. E., Lambert, D. L., et al. 1984, ApJ, 281, 194

Ferland, G. J., Korista, K. T., Verner, D. A., et al. 1998, PASP, 110, 761

Floyd, D. J. E., Kukula, M. J., Dunlop, J. S., et al. 2004, MNRAS, 355, 196

Giacconi, R., Zirm, A., Wang, J., et al. 2002, ApJS, 139, 369

Grevesse, N., & Anders, E. 1989, in AIP Conf. Proc. 183, Cosmic Abundance of Matter, ed. C. J. Waddington (New York: AIP), 1

Grevesse, N., & Noels, A. 1993, in Origin and Evolution of the Elements, ed. N. Prantzos, E. Vangioni-Flam, & M. Casse (Cambridge Univ. Press), 15

Groves, B. A., Dopita, M. A., & Sutherland, R. S. 2004a, ApJS, 153, 9

Groves, B. A., Dopita, M. A., & Sutherland, R. S. 2004b, ApJS, 153, 75

Hamann, F., & Ferland, G. J. 1992, ApJ, 391, L53

Hamann, F., & Ferland, G. J. 1993, ApJ, 418, 11

Hamann, F., & Ferland, G. J. 1999, ARA&A, 37, 487

Hamann, F., Korista, K. T., Ferland, G. J., Warner, C., & Baldwin, J. A. 2002, ApJ, 564, 592

Ho, L. C., Shields, J. C., & Filippenko, A. V. 1993, ApJ, 410, 567

Iwamuro, F., Motohara, K., Maihara, T., et al. 2003, ApJ, 598, 178

Kaspi, S., Smith, P. S., Netzer, H., et al. 2000, ApJ, 533, 631

Kraemer, S. B., Wu, C. -C., Crenshaw, D. M., & Harrington, J. P. 1994, ApJ, 435, 171

Kuhlbrodt, B., Örndahl, E., Wisotzki, L., & Jahnke, K. 2005, A&A, 439, 497

Labbé, I., Huang, J., Franx, M., et al. 2005, ApJ, 624, L81

Malkan, M. A., & Oke, J. B. 1983, ApJ, 265, 92

Marconi, A., Moorwood, A. F. M., Salvati, M., & Oliva, E. 1994, A&A, 291, 18

Marconi, A., Risaliti, G., Gilli, R., et al. 2004, MNRAS, 351, 169

Mathews, W. G., & Ferland, G. J. 1987, ApJ, 323, 456

Mathur, S. 2000, MNRAS, 314, L17

McAlpine, G. M. 1988, PASP, 100, 65

McCarthy, P. J., Le Borgne, D., Crampton, D., et al. 2004, ApJ, 614, L9

McCarthy, P. J., van Breugel, W., & Kapahi, V. K. 1991, ApJ, 371, 478

McLure, R. J., Kukula, M. J., Dunlop, J. S., et al. 1999, MNRAS, 308, 377

Mehlert, D., Noll, S., Appenzeller, I., et al. 2002, A&A, 393, 809

Murayama, T., & Taniguchi, Y. 1998, ApJ, 503, L115

Nagao, T., Murayama, T., & Taniguchi, Y. 2001a, ApJ, 549, 155

Nagao, T., Murayama, T., & Taniguchi, Y. 2001b, PASJ, 53, 629

Nagao, T., Murayama, T., Taniguchi, Y., & Shioya, Y. 2003, AJ, 125, 1729

Nagao, T., Marconi, A., & Maiolino, R. 2006, A&A, 447, 157

Oliva, E., Salvati, M., Moorwood, A. F. M., & Marconi, A. 1994, A&A, 288, 457

Pettini, M., Shapley, A. E., Steidel, C. C., et al. 2001, ApJ, 554, 981

Pettini, M., Steidel, C. C., Adelberger, K. L., Dickinson, M., & Giavalisco, M. 2000, ApJ, 528, 96

Rodríguez-Ardila, A., Pastoriza, M. G., & Donzelli, C. J. 2000, ApJS, 126, 63

Rosati, P., Tozzi, P., Giacconi, R., et al. 2002, ApJ, 566, 667

Saracco, P., Longhetti, M., Severgini, P., et al. 2005, MNRAS, 357, L40

Scott, J. E., Kriss, G. A., Brotherton, M., et al. 2004, ApJ, 615, 135

Shapley, A. E., Erb, D. K., Pettini, M., Steidel, C. C., & Adelberger, K. L. 2004, ApJ, 612, 108

Shields, J. C., & Kennicutt, R. C., Jr. 1995, ApJ, 454, 807

Snijders, M. A. J., Netzer, H., & Boksenberg, A. 1986, MNRAS, 222, 549

Stern, D., Moran, E. C., Coil, A. L., et al. 2002, ApJ, 568, 71

Szokoly, G. P., Bergeron, J., Hasinger, G., et al. 2004, ApJS, 155, 271

Tecza, M., Baker, A. J., Davies, R. I., et al. 2004, ApJ, 605, L109

Telfer, R. C., Zheng, W., Kriss, G. A., & Davidsen, A. F. 2002, ApJ, 565, 773

Teplitz, H. I., McLean, I. S., Becklin, E. E., et al. 2000, ApJ, 533, L65

Thuan, T. X. 1984, ApJ, 281, 126

van Ojik, R., Röttgering, H. J. A., Miley, G. K., et al. 1994, A&A, 289, 54

Vernet, J., Fosbury, R. A. E., Villar-Martin, M., et al. 2001, A&A, 366, 7

Villar-Martin, M., Tadhunter, C., & Clark, N. 1997, A&A, 323, 21

Zamorani, G., Henry, J. P., Maccacaro, T., et al. 1981, ApJ, 245, 357

Zheng, W., Kriss, G. A., Telfer, R. C., Grimes, J. P., & Davidsen, A. F. 1998, ApJ, 492, 855